Wearable microfluidic patch with integrated capillary valves and pumps for sweat management and multiple biomarker analysis

Hengjie Zhang,[1,2,3] Ye Qiu,[1,2,3] Sihang Yu,[1,2,3] Chen Ding,[4] Jiahui Hu,[1,2,3] Hangcheng Qi,[1,2,3] Ye Tian,[1,2,3] (iD)
Zheng Zhang,[1,2,3] Aiping Liu,[4,a] (iD) and Huaping Wu[1,2,3,a] (iD)

AFFILIATIONS

[1]College of Mechanical Engineering, Zhejiang University of Technology, Hangzhou 310023, People's Republic of China
[2]Key Laboratory of Special Purpose Equipment and Advanced Processing Technology, Ministry of Education and Zhejiang Province,
Zhejiang University of Technology, Hangzhou 310023, People's Republic of China
[3]Collaborative Innovation Center of High-end Laser Manufacturing Equipment (National "2011 Plan"),
Zhejiang University of Technology, People's Republic of China
[4]Key Laboratory of Optical Field Manipulation of Zhejiang Province, Zhejiang Sci-Tech University, People's Republic of China

[a])Authors to whom correspondence should be addressed: liuaiping1979@gmail.com and wuhuaping@gmail.com

ABSTRACT

Wearable sweat sensors are essential for providing insight into human physiological health. The currently developed microfluidic sweat sensors have demonstrated the function of collecting and storing sweat. However, they detect more average concentrations of substances based on time periods, which leads to the fact that *in situ* real-time measurement for multiple biomarkers remains a grand challenge. Here, we propose a wearable epidermal microfluidic patch with integrated microfluidic pumps and micro-valves for accelerated and continuous collection of the sweat, where the micro-pumps ensure the complete separation of old and new sweat for real-time detection of real concentration of biomarkers in sweat. The biomarker concentration at different time periods is detected by introducing a burst valve, which is used to assist in the analysis of the real-time detection. A quantitative relationship between the minimum burst pressure difference required for sequential collection and the size of the microchannel structure is established to overcome the effects of additional resistance at the gas–liquid interface. Additionally, the sensing modules, including sodium ion, chlorine ion, glucose, and pH level in sweat, are integrated into the patch to realize *in situ*, real-time detection of multiple biomarkers in the human sweat, decoding the correlation between changes in substance concentrations and physiological conditions. This work provides a unique and simplifying strategy for developing wearable sweat sensors for potential applications in health monitoring and disease diagnostics.

Published under an exclusive license by AIP Publishing. https://doi.org/10.1063/5.0092084

I. INTRODUCTION

Sweat is a product of metabolic activity carried out by the body and contains various biomarkers (e.g., hydrogen ions, sodium ions, glucose, chloride ions, and so on), which can be used to assess electrolyte balance, blood glucose level, hydration status, and personalized health.[1–6] Wearable sweat sensors are capable of recording critical physiological parameters in a non-invasive manner, thus are regarded as an alternate to blood-based sensors for physiological assessment.[7–14] However, the change in a single substance may be caused by multiple health conditions. For example, varieties in

sodium ion concentration may be induced by electrolyte imbalance, or hypernatremia, and diabetes; exercise depletion may lead to changes in glucose concentration.[15–20] Thus, it is highly desirable to design a sweat sensor that can detect real-time changes of multiple biomarkers, which improves the reliability of health assessment in daily activities. Advances in flexible electronics have opened up new opportunities for the manufacture of sweat collection devices that provide useful biomarker measurements.[21–28] Early efforts utilize a variety of flexible materials as substrates for collecting and storing sweat, such as fibers, paper, and screen-printed sensors.[29–37] These

measurement strategies are unable to separate sweat from the skin, resulting in interference from skin surface chemicals and the inability to distinguish the changes in old and new sweat. In addition, biomarkers within the sweat tend to accumulate in the sensing area due to the rapid evaporation of sweat, resulting in the reduction of the sensing accuracy. To address these limitations, microchannel technology has emerged to significantly reduce contamination and evaporation by directing sweat into microchannels, thereby separating sweat from the skin and storing it in a microfluidic system.[38–42] For instance, the design of highly absorbent polymer valves, traps, and capillary burst valves has been demonstrated in microfluidic devices to achieve sequential collection.[43–52] Among them, the capillary burst valve provides a simplifying strategy for achieving the sequential collection of sweat by merely changing the structure of the channel.[53–59] However, the minimum burst pressure (P) that can realize sequential collection is not further considered through theoretical calculation or experimental observation in the design of capillary burst valves, thereby leading to movement burdens and collection difficulties when an additional P is applied. Additionally, sequential collection and detection of sweat show the average change of substances over a period of time and thus expose limitations of real-time detection. Thus, *in situ* real-time measurements of the

biomarker concentrations in sweat remain a daunting challenge, which requires a unique microchannel design in sweat sensors to effectively improve the capability of sequential collection and accelerated collection.

Here, we introduce the microfluidic pumps and micro-valves into the microfluidic channel that is capable of detecting biomarker concentration in a real-time mode [Fig. 1(a)]. The microfluidic pump contributes to the acceleration of sweat flowing and the improvement of collection efficiency, ensuring temporal consistency of the test sweat with the just secreted one and the reliability of real-time detection. The capillary burst valves are integrated into the microfluidic patch, thereby enabling the sequential collection of sweat for better evaluation of human health. A comprehensive set of theoretical/numerical method and experimental schemes is proposed to quantitatively elucidate the range of minimum burst pressure difference (ΔP) for achieving sequential collection. Multiple sensor modules, including sodium ions, chloride ions, glucose, and pH level, are successfully integrated into the detection areas of the microfluidic patch for simultaneous real-time detection [Fig. 1(b)]. This developed wearable sweat sensor with *in situ* real-time measuring capability opens up an optional path toward health monitoring and disease diagnostics.
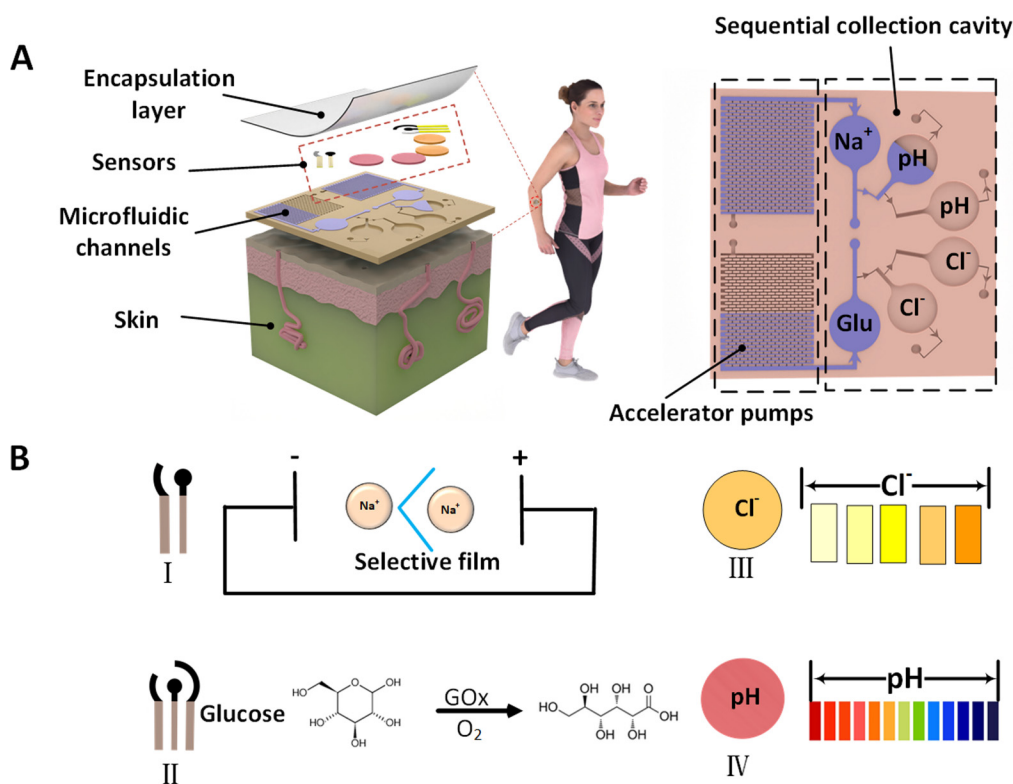
FIG. 1. Schematic diagram of epidermal microfluidic patch with integrated sweat sensors, burst valve and microfluidic pump (accelerator pump). (a) Sensor and microfluidic channel display. (b) Methods for the detection of sodium ions, glucose, chloride ions, and pH level of sweat.

II. EXPERIMENT

A. Materials

Polydimethylsiloxane (PDMS) from Dow Corning, polyimide film (PIF), ferric chloride, potassium chloride, potassium ferricyanide, sodium chloride, hydrochloric acid, methanol, polyvinyl butyral (PVB), polyvinyl chloride (PVC), sodium ionic carrier, tetrahydrofuran, chitosan, potassium tetraborate, bis-decanedioate, phosphate buffer solution (PBS), hydrochloric acid, and glucose oxidase (GOx) were obtained from the Aladdin platform, and the purity of the reagents was analytically pure.

B. Preparation of PDMS microfluidic channels

The stencils with a patterned structure were carved using the SU-8 technique [detailed design in Fig. S1(a) in the supplementary material]. The silicon stencils were cleaned with ethanol solution and then soaked in a mixture of ethyl acetate, *n*-heptane, and dodecamethylsiloxane for 2 h and dried in a fume hood. The purpose of this operation was to make the surface of silicon stencils hydrophobic and easier to peel off the PDMS microfluidic channels after the solution of including PDMS prepolymer was casted onto the stencils with a patterned structure.

C. Preparation of sodium ion sensors

The potentiometric sodium ion sensor consisted of a two-electrode system,[17,19,60–62] namely, a working electrode with a sodium ion selective membrane and a reference electrode with a polyvinyl butyral (PVB) membrane by using the PIF as the substrate. The circle working electrode had a diameter of 2 mm, and the reference electrode was a quarter ring with an inner diameter of 2.2 mm and an outer diameter of 5 mm. The PIF was first washed sequentially with ethanol and de-ionized water, then pasted on the slide. After that, graphene was induced on the PIF surface with CO_2 laser equipment (Shanghai Hehong Laser Equipment Co., Ltd.) at a scanning speed of 150 mm/s. To obtain a sodium ion selective electrode, a mixed solution consisting of dibutyl sebacate, polyvinyl chloride, ethyl 4-*tert*-butyltetraacetate and tetra (4-chlorophenyl) potassium borate (50 mg/ml) was dissolved in the tetrahydrofuran solution, and then 5 µl mixed solution was dropped onto the surface of graphene electrode to form a working electrode. The reference electrode was prepared by applying a silver chloride slurry on the surface of graphene, drying and adding 5 µl of methanol solution (1 ml of methanol solution contained 78.1 mg PVB and 58.5 mg NaCl) on the surface of silver chloride, and the methanol solution was evaporated to form a PVB film on the surface. The sodium ion sensor needed to be soaked in a sodium chloride solution at a concentration of 3 mol/l for half an hour to adjust the potential before use.

D. Preparation of the glucose sensor

The amperometric glucose sensor consisted of three electrodes, in which the Ag/AgCl electrode was used as the reference electrode, the laser-induced graphene (LIG) without modification as the counter electrode, and the modified LIG as the working electrode.[63–65] The working electrode and reference electrode of the glucose sensor were the same as those of the sodium ion sensor. The counter electrode was a ring with an inner diameter of 2.2 mm and an outer diameter of 5 mm. For obtaining the working electrode, the LIG on PIF was placed in the solution containing $K_3[Fe(CN)_6]_2$, $FeCl_3$, HCl, and KCl to electrodeposit Prussian blue film by using the three-electrode system at a constant potential of 0.1 V for 120 s. An agarose membrane emulsion with a mass fraction of 1% agarose and a mass fraction of 1% chitosan solution was prepared in the PBS (pH = 6.5). Then, the solution of GOx oxidase (10 mg/ml), agarose, and chitosan solutions were dropped onto the working electrode to form the glucose sensor with dried overnight at 4 °C for use.

E. Preparation of chlorine ion sensor and pH sensor

The pH sensor was constructed via the commercial test papers (test strip model Q31/0110000034C045) with a 5-mm diameter and placed in the corresponding sensing areas before encapsulation of sweat patch. The reaction cell of pH sensor was treated by plasma to improve the adhesion capacity and ensure the stable combination with pH test strips. For chloride ion sensor preparation, the mercury thiocyanate solution was used to generate colored complexes on the chlorine free test paper,[66] then dried it and put it on the surface of reaction chamber after plasma treatment. pH test strips and chloride test strips did not come into direct contact with the skin.

F. Characteristics

Sodium ion concentration was determined by measuring the open circuit potential (OCP) vs the reference electrode via the electrochemical workstation (CH Instruments, Inc.). The glucose concentration was obtained in PBS using the electrochemical workstation. The role of Prussian blue on the working electrode was to catalyze the decomposition of hydrogen peroxide and generated an electric current. We obtained the maximum reduction peak of Prussian blue at 0.1 V by CV measurement (Fig. S2 in the supplementary material). This potential (0.1 V) was used for glucose measurement by the potentiostatic method to ensure greater catalytic activity of Prussian blue.

Sequential collection and microfluidic pump injection experiments were performed using a syringe pump with an injection rate of 0.025 ml/min. All injected patches were encapsulated with a small opening at the outlet to reduce the back pressure of air in the flowing process of liquid. The COMSOL simulation for sequential collection was carried out by importing a 2D mode with presupposed phase field mode, initial internal filling with air, water injection at the inlet at a constant velocity and contact angle.

III. RESULTS AND DISCUSSION

A. Design and integration of burst valves with minimum burst pressure difference for sequential collection of sweat

The microfluidic channels are symmetrical in structure, comprising three chambers for real-time detection of sodium ion concentration and pH level and an accelerator pump for accelerated collection of sweat [or for real-time detection of chloride ion

concentration and glucose and stepped-up management of sweat, Fig. 1(a)]. In order to achieve sequential collection of sweat, a comprehensive analysis to quantitatively elucidate the range of minimum ΔP is carried out. According to the principle of capillary force, if a large change in the size of channel occurs during the fluid flowing, a large resistance (namely, ΔP) will be generated, which can be expressed by the Young equation

$$\Delta P = P_A - P_O = -4\sigma \frac{\cos \theta_A}{D}. \quad (1)$$

Here, P_A and P_O are the internal and external capillary pressures at the surface of bent liquid in the round channel [Fig. S1(b) in the supplementary material], respectively; σ is the surface tension of the liquid; θ_A is the contact angle between the liquid and the wall of the channel as it advances; D is the capillary diameter. In the rectangular tube, the ΔP can be calculated using the following Young-type equation:

$$\Delta P = P_A - P_O = -\sigma \left(\frac{\cos \theta_l + \cos \theta_r}{w} + \frac{\cos \theta_t + \cos \theta_b}{h} \right), \quad (2)$$

where $\cos \theta_b$, $\cos \theta_r$, $\cos \theta_t$, and $\cos \theta_b$ are the contact angles of the liquid in the left, right, top, and bottom surfaces of the rectangular channel, respectively; w and h are the width and height of the channel [Fig. S1(c) in the supplementary material], respectively. In the preparation process of burst valve, the defects produced in the preparation process will affect the performance of the burst valve, so the use of rectangular channel and burst valve with round chamfer can extend the dispersion angle and make it easier to control the ΔP. We use uniform material to control the contact angle, at this point the equation with dispersion angle θ_I is given as

$$\Delta P = P_A - P_O = -\sigma \left(\frac{\cos \theta_I}{w^\star} + \frac{\cos \theta_I}{h} \right). \quad (3)$$

Here, $w^\star = w + 2r_e(1 - \cos \beta)$, r_e denotes the radius of the circle chamfer of rectangular channel, β denotes the angle of widening at the through circle chamfer [Fig. S1(d) in the supplementary material], $\theta_I = \min\{\theta_A + \beta, 180°\}$.

The validation experiment for sequential collection was carried out by using the model including two valves with different P, three chambers, and one inlet and one outlet [Fig. 2(a)]. In solving for the minimum ΔP to achieve sequential collection, we set different adjacent pressure differences to be filled. Four sets of experiments were carried out (experiment details shown in Figs. S3–S5 in the supplementary material) and a minimum ΔP between 125 Pa and 150 Pa for sequential collection is obtained. The filling time at a set burst pressure ($\Delta P = 150$ Pa) with a filling rate of 0.025 ml/min is about 79 s, and four sets of control tests show similar results [Fig. 2(c) and Fig. S6 in the supplementary material]. We also fit the experimental and theoretically calculated ΔP [Fig. 2(b) and Fig. S1(d) in the supplementary material, w_1, w_2 and w_2 in Fig. S1(d) in the supplementary material are passage dimensions of the rupture valves], where the red dots indicate the widths of flow path for sequential burst, the gray dots indicate the width of flow path for simultaneous burst, and the orange and cyan

dividing line roughly demonstrates the relationship between the widths of flow paths for adjacent burst valves when sequential bursts are desired. The results in Fig. 2(b) illustrate that through the fitting of experimental and theoretical simulations, we have obtained a minimum relationship between the widths of adjacent burst valves that should satisfy when the sequential bursting can be achieved. The simulation of flowing process of the fluid was also carried out based on the designed structure and presents similar flowing tendency to the experimental results [Fig. 2(d) and Movie S1 in the supplementary material]. This suggests that the reasons for sequential bursting are the variations in channel structures which provide different burst pressures. Therefore, a combination of theory, experiment and simulation has enabled us to derive an approximate range of minimum ΔP and the relationship between adjacent channels with different burst valves, which will assist in the design of subsequent burst valves.

## B. Design and integration of microfluidic pumps for acceleration collection of sweat

The flow rate of sweat in the channel affects the sensor's performance in detecting human health in real time; therefore, it is particularly important to ensure a rapid flowing of sweat through the detection zone during sweat detection. Here, we propose and design a microfluidic pump to accelerate the flowing of sweat through the microchannel (Fig. 3). The principle of microfluidic pumping is to construct more hydrophilic channel surface to achieve the positive driving effect of capillary force on the liquid by arranging the microcolumn arrays in the channel [Figs. S1(a) and S7 in the supplementary material], which can provide a larger contact area for the capillary force and achieve a longer driving effect. The flowing of liquid in the microfluidic channel is characterized by a reduction in the solid–air area, an increase in the solid–liquid area and a change in the free energy of the surface (Fig. S7 in the supplementary material). The Gibbs free energy G of the system during the microfluidic wetting process can be expressed as

$$G = \sum_{i=t,b,l,r} (\gamma_{LV_i} \Delta S_{LV_i} + \gamma_{SV_i} \Delta S_{SV_i} + \gamma_{SL_i} \Delta S_{SL_i}). \quad (4)$$

Here, t, b, l, and r represent the top, bottom, left, and right walls of the channel, respectively; γ_{LV_i}, γ_{SV_i} and γ_{SL_i} represent the surface tensions at the liquid-gas, solid–gas, and solid–liquid interfaces, respectively; ΔS_{LV_i}, ΔS_{SV_i}, and ΔS_{SL_i} represent the contact areas at the liquid–gas, solid–gas, and solid–liquid interfaces, respectively. The process of wetting the channels by liquids is characterized by an increase in the contact area of the solid–liquid and a decrease in the contact area of the solid–gas, then G in the filling process can be expressed as

$$G = (\gamma_{SV_t} - \gamma_{SL_t}) \times \Delta S_{SV_t} + (\gamma_{SV_b} - \gamma_{SL_b}) \times \Delta S_{SV_b} + 2 \times (\gamma_{SV_r} - \gamma_{SL_r}) \times \Delta S_{SV_r}. \quad (5)$$

Combining the Young-type equation ($\gamma_{SV_i} - \gamma_{SL_i} = \gamma_{LV_i} \times \cos \theta_{A_i}$, $i = t, b, l, r$), the relation of G and capillary pressure P ($G = P \times V$, V is the volume of the flow channel) and Eq. (5), P of
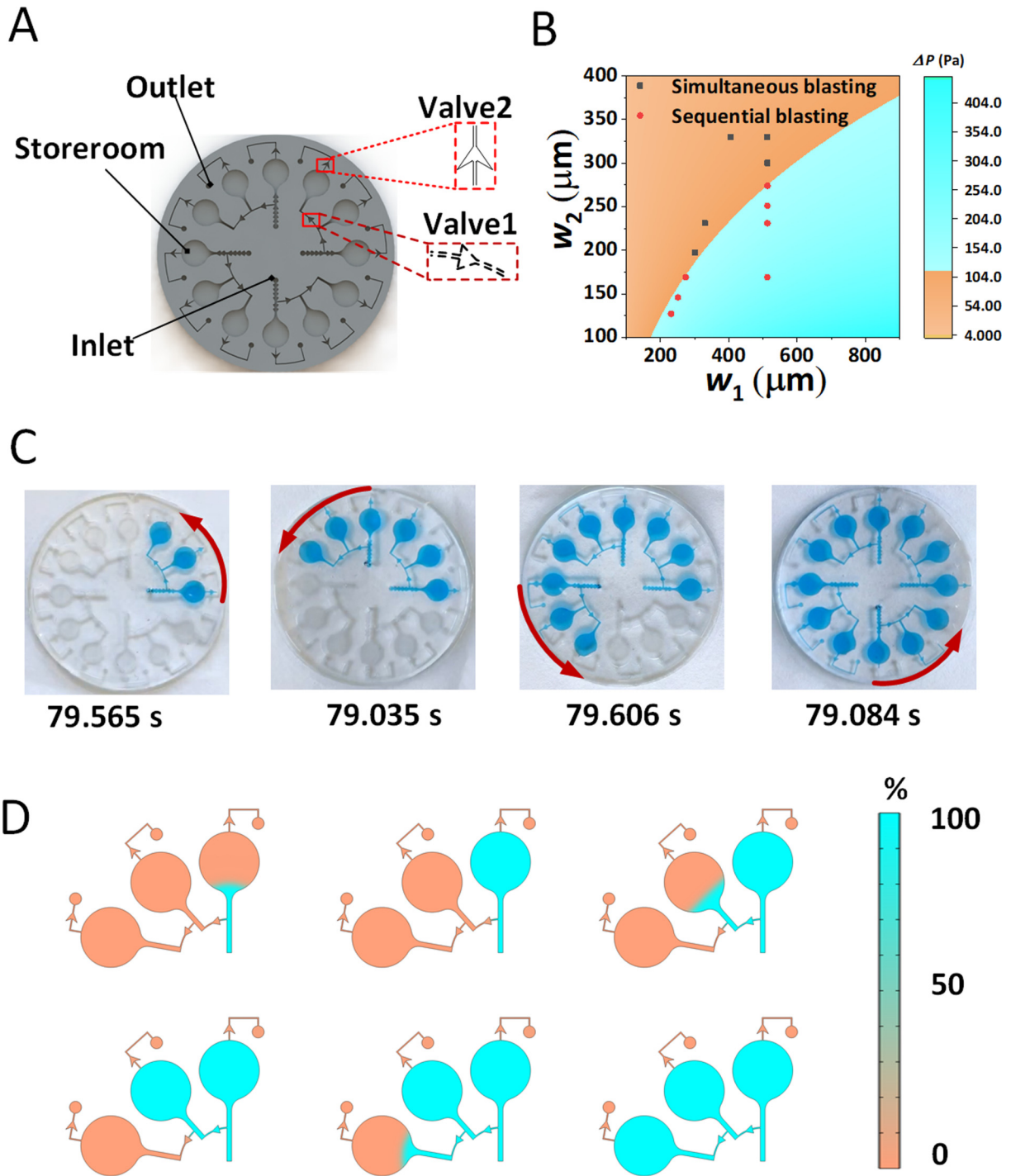
FIG. 2. Design of the burst valves for sequential collection test. (a) Three-dimensional construction of the burst valve. (b) Theoretical calculated phase diagram of ΔP generated by adjacent burst valves with different sizes (w_1 and w_2 were the widths of flow path for burst valves) and the comparison with experimental results for sequential collection. The red dots and gray dots indicated the widths of flow paths for sequential burst and simultaneous burst, respectively. The orange and cyan dividing line demonstrated the relationship between the widths of adjacent burst valves when sequential bursts were desired. (c) Time spent in four control experiments when sequential bursting occurrence ($\Delta P = 150$ Pa). (d) Filling process of the liquid under COMSOL simulation when sequential bursting occurrence.
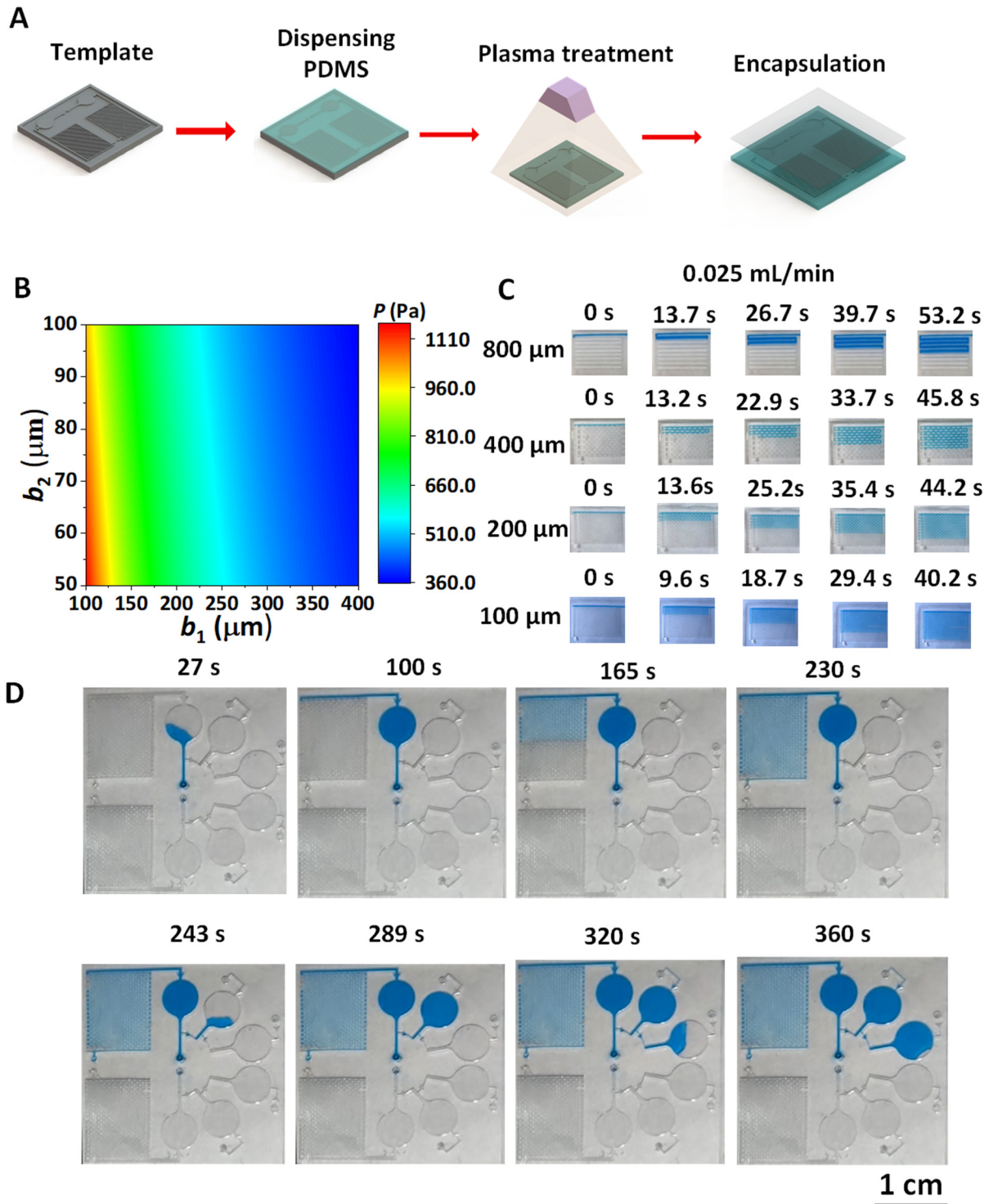
FIG. 3. Design and integration of microfluidic pumps. (a) Preparation and structure of microfluidic pump. (b) Phase diagram of the driving pressure for the microfluidic pump with different width sizes. (c) Time required to flow through the same volume of microfluidic pump with different main flow channel widths (b_1) between adjacent microcolumns. (d) Experimental diagrams of the flowing process of liquid in the sweat patch integrated microfluidic pump and rupture valves.

the capillary microfluidic pump can thus be given as

$$P = \frac{\gamma_{LV_t} \times (\cos\theta_t \times \Delta S_{SV_t} + \cos\theta_b \times \Delta S_{SV_b} + 2^\star\cos\theta_r \times \Delta S_{SV_r})}{V}.$$

$$(6)$$

We fix the microcolumn length $L = 0.7$ mm, width $b_3 = 0.1$ mm, height $h = 0.3$ mm, change the dimensions of b_1 (main flow channel width between adjacent microcolumns) and b_2 (side flow channel width between adjacent microcolumns) [Fig. S1(a) in the supplementary material], and calculate P generated at the pumps with different channel widths [Fig. 3(b)]. The result shows that P increases with b_1 and b_2 decrease, which is very helpful for obtaining fast flowing characteristics of microfluidics in the microfluidic pump. In order to verify the structure effect of microfluidic pump on the flowing behavior of sweat in the channel, the microfluidic pumps with the same h and alterable b_1 ($b_1 = 0.1, 0.2, 0.4,$ and 0.8 mm) and b_2 ($b_2 = 0.05, 0.1,$ and 0.2 mm) were prepared and treated hydrophilically by a plasma machine [Fig. 3(a)]. When the liquid is injected into the channel as a filling rate of 0.025 ml/min, experimental results agree well with those of theoretical ones, namely, the smaller the b_1, the shorter the relative time required to flow through the same volume [Fig. 3(c)]. The flowing speeds of liquid in the channel with different structures are therefore obtained, namely, 0.288 ml/min at $b_1 = 0.8$ mm, 0.312 ml/min at $b_1 = 0.4$ mm, 0.324 ml/min at $b_1 = 0.2$ mm, and 0.384 ml/min at $b_1 = 0.1$ mm. Finally, we integrate the microfluidic pump with the burst valves in the sweat patch [Fig. 1(a), Fig. S8 in the supplementary material]. The roles of valve2 and valve3 are to achieve the sequential collection of liquid, and the role of valve1 is to ensure that the liquid can fill the reaction chamber before entering the microfluidic pump. The microfluidic pump behind one of the chambers serves as an accelerator for accelerated collection of the liquid in order to completely separate old and new sweat for real-time detection of real biomarker concentration of sweat [Fig. 3(d), Movie S2 in the supplementary material]. When the microfluidic pump is integrated at the end of chamber 1, chambers 2 and 3 are not affected by the driving force. The position of the microfluidic pump is convenient and flexible to change according to specific needs for real reflection of the concentration changes of substances in the sweat in different time frames.

In the entire microfluidic patch, the width of the micropath connected to the reaction chamber is $400\,\mu$m, which prevents the channel from generating a large resistance when entering the reaction chamber, and the remaining micropath width is $100\,\mu$m, which can achieve the maximum driving effect in the channel. The area of each reaction chamber is about 19.6 mm^2, which can be filled with about $5.9\,\mu$l of sweat. After the complete reaction chamber is filled with sweat, the sweat can be discharged from the outlet due to the greater pressure of the burst valve (valve 3) at the outlet than that at the sequential burst, so the burst valve at the outlet is the last to break through.

C. *In vitro* multicomponent detection via the epidermal microfluidic patch

The sensing and detection capacity of epidermal microfluidic patch to sodium ions, chloride ions, glucose, and pH level was first investigated by the *in vitro* test via the microfluidic patch [Figs. 1(b) and 4]. Each substance was determined for six times to investigate the sensor stability and reproducibility. The sodium ion sensor consists of a two-electrode system and the glucose sensor consists of a three-electrode system [Figs. 1(b) and 5(a)]. The detection principle of sodium ions via the electrochemical system is that the anion neutral carrier accelerates the gathering of cations near the anode, the sodium ion selective carriers selectively allow the sodium ions to pass through and the increased voltage is related to the concentration of sodium ions. The PVB wrapped reference electrode ensures the stability of the electrode. The principle of glucose detection is that glucose is oxidized on the working electrode to form hydrogen peroxide, which is further decomposed by Prussian blue to produce an electric current.[67] The sodium ion and glucose sensors were calibrated and tested separately. The sodium ion sensor exhibits different potential signals in the Na$^+$ concentrations from 20 to 200 mm with good resolution and stability, and the linearity of the sodium ion sensor is 0.055 04 V/Deced and is in accordance with the Nernst equation law [Fig. 4(a)]. The equation for calculating the energy of the sodium ion is

$$E(\text{Na}^+) = \varphi(\text{Standard}) + \frac{0.0592}{2}\log(\text{Na}^+). \qquad (7)$$

The glucose sensor exhibits different electrical signals in the glucose concentrations from 50 to 200 μM with good discrimination. The color changes of test papers vs pH level or Cl$^-$ concentration in the pH and chloride ion sensors are shown in Fig. 4(c), thereby verifying good combination of test papers and microfluidic patch. All detection limits already include the ranges of human substance concentrations.

D. On-body multicomponent analysis of sweat via the epidermal microfluidic patch

To demonstrate the effectiveness of the sweat sensor in the microfluidic patch, we attached it to the wrist of six volunteers for multicomponent analysis of sweat under arm movement [Fig. 5(a)]. Before the start of the experiment, the volunteer will drink 200 ml of 60 °C normal saline, and the ambient temperature will be adjusted to 30 °C to ensure the sweating effect. We show the changes of sodium ion and glucose concentrations of the human body during one hour of sweating, with results read every 5–10 min [Fig. 5(b)]. The results show a decrease in glucose concentration during the first 20 min of exercise and an increase in glucose concentration after 20 min. Some reports suggest that the glucose concentration in sweat is closely associated with blood glucose concentration, the initial exercise usually produces a depletion of glucose, while the release of cortisol hormone during subsequent exercise will lead to an increase in blood glucose,[68,69] therefore presenting increased glucose concentrations in sweat. The sodium ion concentration in sweat displays a continuous growth in the whole process of motion due to electrolyte loss from the body. All detection results of multicomponent analysis of sweat in our on-body measurement are within the normal sweat composition range.[40] We also integrated pH and chloride colorimetric sensors in the sequential collection chamber to observe the time taken for
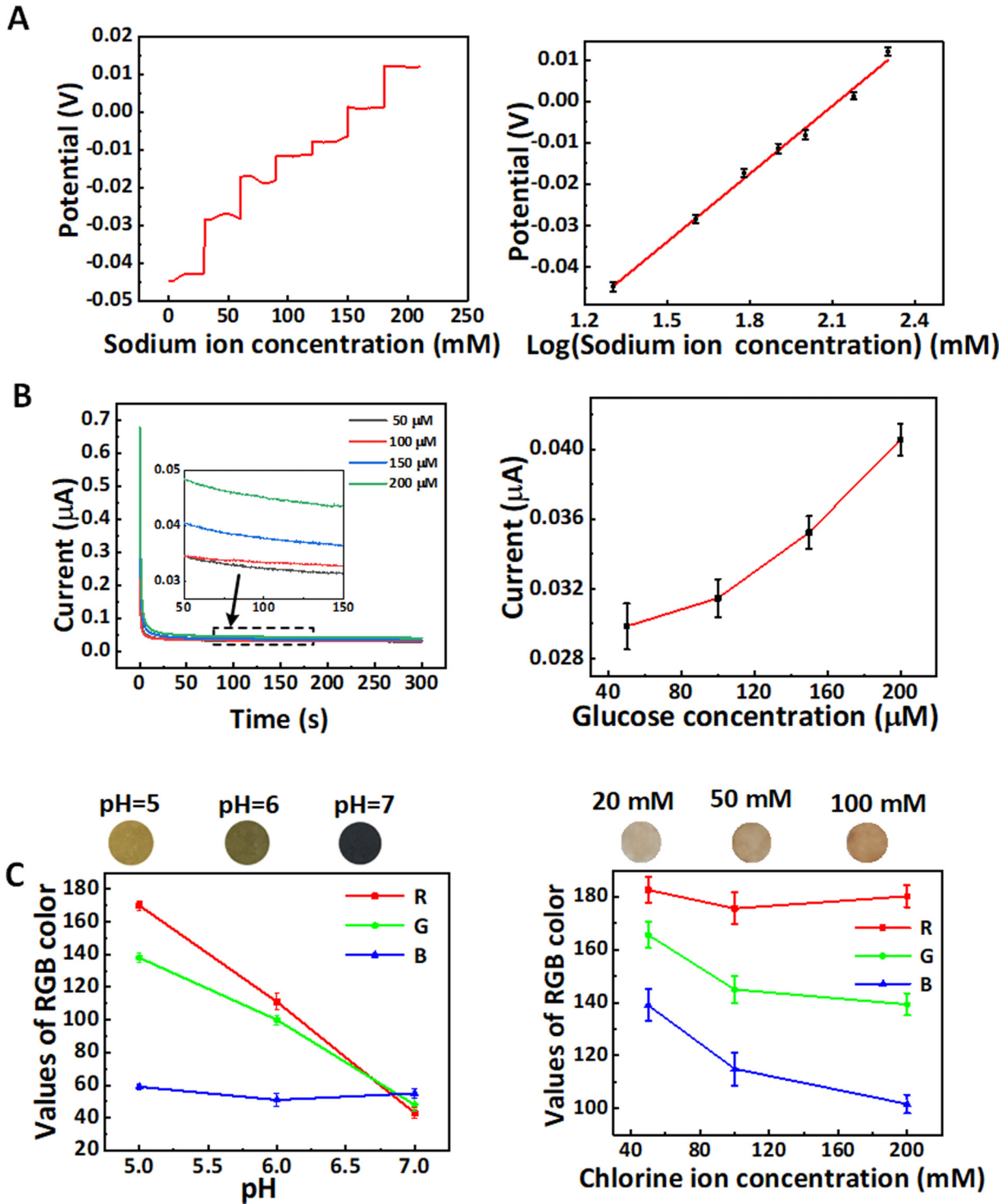
FIG. 4. *In vitro* multicomponent detection via the epidermal microfluidic patch. (a) Relation of open circuit potential and Na$^+$ concentration and the linearity of sodium ion sensor ($R^2 = 0.992$). (b) Relation of oxidation current and glucose concentration and the calibration of glucose sensor. (c) Colorimetric calibration chart for pH level and chloride ion concentration by using the pH and chloride ion sensors. The error bars for all data were the standard deviation of repeated measurement.
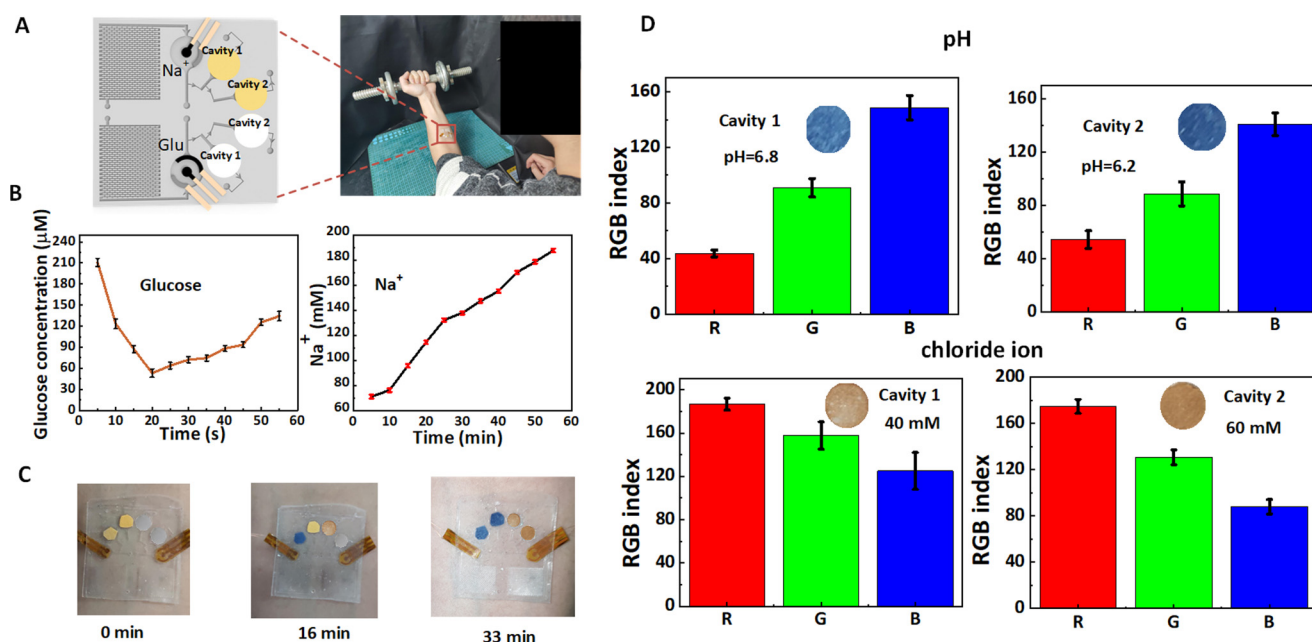
FIG. 5. On-body sweat analysis via the epidermal microfluidic patch. (a) Schematic diagram of the integrated sweat sensor for multicomponent analysis of sweat under arm movement. (b) Assay signals of sodium ion and glucose concentrations during one-hour exercise. (c) Color change on colorimetric stickers for the pH assay with passage of time. (d) pH and chloride ion concentration of sweat in two cavities were detected for different individuals.

the liquid to fill sequentially and the colorimetric situation at the end of real-time sensing. pH and chloride ions test strips produce colorimetric reactions after direct contact with the sweat [Figs. 5(c) and 5(d)]. Then, the color changes of test strips were recorded by the camera and analyzed via the Color Picker function in Pixolor software to obtain the RGB value of the test strips and compare with the RGB value in the standard colorimetric card (the color of test strips for the known concentration or pH of solution was given) to obtain the corresponding concentration and pH range. The results show that the pH value displays a slight but not significant decrease, indicating that the body's metabolic status remains stable. The concentration of chloride ions is gradually increasing just like that of sodium ions, concluding that the body is losing water.[70] According to the ratio of volume to time of patch design, we obtain that the average sweating rate in the channel is about 0.58 μl/min, which is higher than those in previous studies.[41,71] This average sweating rate of the sweat is lower than that of test liquid in the channel with different structures (Sec. III B), indicating that the microfluidic pump can act as an accelerator to realize the sweat control.

To further demonstrate the *in situ* driving effect of the microfluidic pump on sweat, we set up flow channels with and without microcolumns. The flow channels without microcolumns have the width of 800 μm [left in Fig. S9(a) in the supplementary material] and 100 μm [left in Fig. S9(b) in the supplementary material], respectively, when they have the same height and holding capacity. While the flow channel with microcolumns has a width about 100 μm [right in Figs. S9(a) and S9(b) in the supplementary

material] and an additional 27 μl holding capacity due to the gap between the microcolumn arrays. Then, we installed the sodium ion sensors in the reaction chambers of microfluidic patch for real-time sweat detection to determine the effect of microfluidic pump [Figs. S9(a) and S9(b) in the supplementary material]. The sweat inlets of the two structures were separated by 2 mm to reduce measurement errors caused by the different sites. Two microfluidic patches were fixed to the wrists of six volunteers for analyzing the Na$^+$ concentration in sweat under arm movement. Before the experiment started, the volunteers drank 200 ml of normal saline at 60 °C and the ambient temperature was adjusted to 30 °C to ensure the sweating effect. As shown in Fig. S9(c) in the supplementary material, after 10 min of sweating, there is a significant numerical difference obtained from two flow channels without microcolumns. This is because that the new sweat and the old sweat are more easily mixed in the 800 μm-width flow channel and the assay results tend to be the average concentration at some point in time. By contrast, the flow channel with the microcolumn arrays is less prone to mixing the old and new sweat [Fig. S9(c) in the supplementary material] because it could hold more sweat volume in the same length of the flow channel, thus reducing the problem of excessive resistance due to insufficient driving force caused by the increased length of flow channel. The theoretical equation for the increase of resistance with length in the flow channel is[72]

$$R_{\mathrm{f}} = \frac{12\,\mu L}{wh^3}, \tag{8}$$

where R_f denotes the flow resistance of the droplet, μ indicates the viscosity of the droplet, w and h denote the width and height of the channel, respectively, and L is the length of the channel. Therefore, our data indicate that the microfluidic pump in the microfluidic patch works well *in situ* condition on the skin.

In short, our sweat sensing patch with microfluidic control provides rapid filling of the channel to guide and separate the old from the new sweat, allowing for changes in sweat substance concentration during continuous exercise. The sodium ion and glucose sensors demonstrate the difference in the amount of substance that occurs in healthy humans during one hour of exercise and match the predicted water loss and energy expenditure of the human body during exercise. Chambers with sequential bursts collect sweat over different time periods and colorimetric sensors in both chambers show subtle differences in the body's acid-base concentration. Combining the quantitative and qualitative tests, we can see that the change in substance concentration is due to water loss and increased cortisol hormone following exercise.

The sweat patch developed in this paper is a wearable patch, and its signal transmission and reception can be carried out through wireless transmission via Bluetooth and Zigbee, and the cell phones via the sido interface. In addition, a power is necessary for the electrochemical sensor to generate current and voltage signals, so a signal conversion interface is needed to convert the electrical signal into a digital signal before the wireless transmission. All equipment components for data processing and transmission can be integrated within a Flexible Printed Circuit Board (FPCB) to achieve real-time information detection and signal transmission.

IV. CONCLUSION

By integrating a microfluidic pump with a rupture valve into the microfluidic channel, we achieved a directed and rapid flow of sweat within the channel in an epidermal microfluidic patch. The design of the burst valve not only allows for sequential sampling of sweat, but also does not add excessive burst resistance (125–150 Pa). The microfluidic pump enables rapid outflow of old sweat from the sensing area and rapid inflow of new sweat, ensuring the reliability of real-time detection. Both the microfluidic pump and the rupture valve are prepared by changing the structure within the channel, allowing the structural parameters to be varied according to the expected fill rate and fill sequence, ensuring stability of the acceleration and sequential collection functions without the need to add additional material. Electrochemical sensing and colorimetric sensing as our functional demonstration modules show the patch's ability to combine well with both detection methods, which can reduce the difficulty of sensor preparation while improving the accuracy as well as reliability of detection, and the co-detection of multiple substances provides more convincing evidence of changes in human physiological conditions. Our work opens another path for the development of wearable sensors and health detection and disease diagnosis.

SUPPLEMENTARY MATERIAL

See the supplementary material for more graphical and numerical data and detailed analysis (Figs. S1–S9), and movie

illustration for the simulation of flowing process (Movie S1) and experimentally accelerated and sequential collection of the liquid in the microfluidic channels (Movie S2).

AUTHOR DECLARATIONS

Conflict of Interest

The authors have no conflict to disclose.

Author Contributions

Hengjie Zhang: Formal analysis (equal); Methodology (equal); Software (equal); Writing – original draft (equal). **Ye Qiu:** Data curation (equal); Formal analysis (equal); Methodology (equal). **Sihang Yu:** Data curation (equal); Software (equal). **Chen Ding:** Methodology (equal). **Jiahui Hu:** Methodology (equal). **Hangcheng Qi:** Data curation (equal); Methodology (equal). **Ye Tian:** Formal analysis (equal); Methodology (equal). **Zheng Zhang:** Formal analysis (equal); Methodology (equal). **Aiping Liu:** Supervision (equal); Writing – review & editing (equal). **Huaping Wu:** Investigation (equal); Writing – review & editing (equal).

DATA AVAILABILITY

The data that support the findings of this study are available from the corresponding author upon reasonable request.

REFERENCES

[1] M. Al-Omari, K. Sel, A. Mueller, J. Edwards, and T. Kaya, J. Appl. Phys. **115**, 203107 (2014).

[2] C. Park, C. Stafford, and W. Lockette, Chest **134**, 552–558 (2008).

[3] D. R. Seshadri, R. T. Li, J. E. Voos, J. R. Rowbottom, C. M. Alfes, C. A. Zorman, and C. K. Drummond, Npj Digit. Med. **2**, 72 (2019).

[4] M. Bariya, H. Y. Y. Nyein, and A. Javey, Nat. Electron. **1**, 160–171 (2018).

[5] M. J. Buono, K. D. Ball, and F. W. Kolkhorst, J. Appl. Physiol. **103**, 990–994 (2007).

[6] M. J. Buono, M. Kolding, E. Leslie, D. Moreno, S. Norwood, A. Ordille, and R. Weller, J. Therm. Biol. **71**, 237–240 (2018).

[7] A. J. Bandodkar and J. Wang, Trends Biotechnol. **32**, 363–371 (2014).

[8] R. Ghaffari, J. A. Rogers, and T. R. Ray, Sens. Actuators B **332**, 129447 (2021).

[9] Y. R. Yang and W. Gao, Chem. Soc. Rev. **48**, 1465–1491 (2019).

[10] Y. R. Yang, Y. Song, X. J. Bo, J. H. Min, O. S. Pak, L. L. Zhu, M. Q. Wang, J. B. Tu, A. Kogan, H. X. Zhang, T. K. Hsiai, Z. P. Li, and W. Gao, Nat. Biotechnol. **38**, 217–224 (2020).

[11] H. Lee, C. Song, Y. S. Hong, M. S. Kim, H. R. Cho, T. Kang, K. Shin, S. H. Choi, T. Hyeon, and D. H. Kim, Sci. Adv. **3**, e1601314 (2017).

[12]M. Chung, G. Fortunato, and N. Radacsi, J. R. Soc. Interface **16**, 20190217 (2019).

[13]C. G. Wu, X. Zhang, R. Wang, L. J. Chen, M. Nie, Z. Q. Zhang, X. D. Huang, and L. Han, Nanotechnology **33**, 072001 (2022).

[14]W. A. D. M. Jayathilaka, K. Qi, Y. L. Qin, A. Chinnappan, W. Serrano-Garcia, C. Baskar, H. B. Wang, J. X. He, S. Z. Cui, S. W. Thomas, and S. Ramakrishna, Adv. Mater. **31**, 1805921 (2019).

[15]A. H. Eckhard, M. Zhu, J. T. O'Malley, G. H. Williams, J. Loffing, S. D. Rauch, J. B. Nadol, M. C. Liberman, and J. C. Adams, Acta Neuropathol. **137**, 343–357 (2019).

[16]P. M. Farrell, B. J. Rosenstein, T. B. White, F. J. Accurso, C. Castellani, G. R. Cutting, P. R. Durie, V. A. LeGrys, J. Massie, R. B. Parad, M. J. Rock, and P. W. Campbell, J. Pediatr. **153**, S4–S14 (2008).

[17]A. J. Bandodkar, D. Molinnus, O. Mirza, T. Guinovart, J. R. Windmiller, G. Valdes-Ramirez, F. J. Andrade, M. J. Schoning, and J. Wang, Biosens. Bioelectron. **54**, 603–609 (2014).

[18]Y. Hatamoto, R. Goya, Y. Yamada, E. Yoshimura, S. Nishimura, Y. Higaki, and H. Tanaka, J. Appl. Physiol. **123**, 278–284 (2017).

[19]E. K. Wujcik, N. J. Blasdel, D. Trowbridge, and C. N. Monty, IEEE Sens. J. **13**, 3430–3436 (2013).

[20]Z. Yuan, L. Hou, M. Bariya, H. Y. Y. Nyein, L. C. Tai, W. B. Ji, L. Liabc, and A. Javey, Lab Chip **19**, 3179–3189 (2019).

[21]Y. Qiu, C. Wang, X. Lu, H. Wu, X. Ma, J. Hu, H. Qi, Y. Tian, Z. Zhang, G. Bao, H. Chai, J. Song, and A. Liu, Adv. Funct. Mater. **32**, 2110296 (2022).

[22]D. P. Rose, M. E. Ratterman, D. K. Griffin, L. Hou, N. Kelley-Loughnane, R. R. Naik, J. A. Hagen, I. Papautsky, and J. C. Heikenfeld, IEEE Trans. Biomed. Eng. **62**, 1457–1465 (2015).

[23]Y. Qiu, S. S. Sun, C. Xu, Y. Y. Wang, Y. Tian, A. P. Liu, X. Hou, H. Chai, Z. Zhang, and H. P. Wu, J. Mater. Chem. C **9**, 584–594 (2021).

[24]W. Gao, H. Ota, D. Kiriya, K. Takei, and A. Javey, Acc. Chem. Res. **52**, 523–533 (2019).

[25]Y. Qiu, Y. Tian, S. S. Sun, J. H. Hu, Y. Y. Wang, Z. Zhang, A. P. Liu, H. Y. Cheng, W. Z. Gao, W. N. Zhang, H. Chai, and H. P. Wu, Nano Energy **78**, 105337 (2020).

[26]C. Shi, Z. Zou, Z. Lei, P. Zhu, W. Zhang, and J. Xiao, Sci. Adv. **6**, eabd0202 (2020).

[27]H. Zhou, Y. Zhang, Y. Qiu, H. Wu, W. Qin, Y. Liao, Q. Yu, and H. Cheng, Biosensors Bioelectron. **168**, 112569 (2020).

[28]X. Ning, X. Yu, H. Wang, R. Sun, R. E. Corman, H. Li, C. M. Lee, Y. Xue, A. Chempakasseril, Y. Yao, Z. Zhang, H. Luan, Z. Wang, W. Xia, X. Feng, R. H. Ewoldt, Y. Huang, Y. Zhang, and J. A. Rogers, Sci. Adv. **4**, eaat8313 (2018).

[29]X. Wang, J. A. Hagen, and I. Papautsky, Biomicrofluidics **7**, 014107 (2013).

[30]Q. Cao, B. Liang, T. Tu, J. Wei, L. Fang, and X. Ye, RSC Adv. **9**, 5674–5681 (2019).

[31]M. Parrilla, T. Guinovart, J. Ferre, P. Blondeau, and F. J. Andrade, Adv. Healthcare Mater. **8**, 1900342 (2019).

[32]M. M. Y. R. Riad and A. R. Eldamak, IEEE Access **8**, 177757–177766 (2020).

[33]W. He, C. Wang, H. Wang, M. Jian, W. Lu, X. Liang, X. Zhang, F. Yang, and Y. Zhang, Sci. Adv. **5**, eaax0649 (2019).

[34]S. S. Wu, Z. J. Shao, H. Xie, T. Xiang, and S. B. Zhou, J. Mater. Chem. A **9**, 1048–1061 (2021).

[35]C. H. Liu, T. L. Xu, D. D. Wang, and X. J. Zhang, Talanta **212**, 120801 (2020).

[36]V. Mazzaracchio, A. Serani, L. Fiore, D. Moscone, and F. Arduini, Electrochim. Acta **394**, 139050 (2021).

[37]T. Shay, T. Saha, M. D. Dickey, and O. D. Velev, Biomicrofluidics **14**, 034112 (2020).

[38]H. Y. Y. Nyein, L.-C. Tai, N. Quynh Phuong, M. Chao, G. B. Zhang, W. Gao, M. Bariya, J. Bullock, H. Kim, H. M. Fahad, and A. Javey, ACS Sensors **3**, 944–952 (2018).

[39]J. T. Reeder, Y. G. Xue, D. Franklin, Y. J. Deng, J. Choi, O. Prado, R. Kim, C. Liu, J. Hanson, J. Ciraldo, A. J. Bandodkar, S. Krishnan, A. Johnson, E. Patnaude, R. Avila, Y. G. Huang, and J. A. Rogers, Nat. Commun. **10**, 5513 (2019).

[40]A. Koh, D. Kang, Y. Xue, S. Lee, R. M. Pielak, J. Kim, T. Hwang, S. Min, A. Banks, P. Bastien, M. C. Manco, L. Wang, K. R. Ammann, K.-I. Jang, P. Won, S. Han, R. Ghaffari, U. Paik, M. J. Slepian, G. Balooch, Y. Huang, and J. A. Rogers, Sci. Transl. Med. **8**, 366ra165 (2016).

[41]Z. Sonner, E. Wilder, J. Heikenfeld, G. Kasting, F. Beyette, D. Swaile, F. Sherman, J. Joyce, J. Hagen, N. Kelley-Loughnane, and R. Naik, Biomicrofluidics **9**, 031301 (2015).

[42]L. Wei, G. Fang, Z. Kuang, L. Cheng, H. Wu, D. Guo, and A. Liu, Sens. Actuators B **353**, 131085 (2022).

[43]Y. Zhang, Y. Chen, J. Huang, Y. Liu, J. Peng, S. Chen, K. Song, X. Ouyang, H. Cheng, and X. Wang, Lab Chip **20**, 2635–2645 (2020).

[44]S. B. Kim, Y. Zhang, S. M. Won, A. J. Bandodkar, Y. Sekine, Y. G. Xue, J. Koo, S. W. Harshman, J. A. Martin, J. M. Park, T. R. Ray, K. E. Crawford, K. T. Lee, J. Choi, R. L. Pitsch, C. C. Grigsby, A. J. Strang, Y. Y. Chen, S. Xu, J. Kim, A. Koh, J. S. Ha, Y. G. Huang, S. W. Kim, and J. A. Rogers, Small **14**, 1703334 (2018).

[45]J. Choi, D. Kang, S. Han, S. B. Kim, and J. A. Rogers, Adv. Healthcare Mater. **6**, 1601355 (2017).

[46]S. Jo, D. Sung, S. Kim, and J. Koo, Biomed. Eng. Lett. **11**, 117–129 (2021).

[47]A. R. Naik, B. Warren, A. Burns, R. Lenigk, J. Morse, A. Alizadeh, and J. J. Watkins, Microfluid. Nanofluid. **25**, 2 (2021).

[48]A. J. Bandodkar, J. Choi, S. P. Lee, W. J. Jeang, P. Agyare, P. Gutruf, S. Q. Wang, R. A. Sponenburg, J. T. Reeder, S. Schon, T. R. Ray, S. L. Chen, S. Mehta, S. Ruiz, and J. A. Rogers, Adv. Mater. **31**, 1902109 (2019).

[49]J. Xiao, Y. Liu, L. Su, D. Zhao, L. Zhao, and X. Zhang, Anal. Chem. **91**, 14803–14807 (2019).

[50]Y. Liu, M. Cheng, J. Huang, Y. Liu, Y. Chen, Y. Xiao, S. Chen, X. Ouyang, H. Cheng, and X. Wang, ACS Appl. Mater. Interfaces **13**, 36849–36858 (2021).

[51]J. Choi, D. Kang, S. Han, S. B. Kim, and J. A. Rogers, Adv. Healthcare Mater. **6**, 1601355 (2017).

[52]A. J. Bandodkar, P. Gutruf, J. Choi, K. Lee, Y. Sekine, J. T. Reeder, W. J. Jeang, A. J. Aranyosi, S. P. Lee, J. B. Model, R. Ghaffari, C. J. Su, J. P. Leshock, T. Ray, A. Verrillo, K. Thomas, V. Krishnamurthi, S. Han, J. Kim, S. Krishnan, T. Hang, and J. A. Rogers, Sci. Adv. **5**, eaav3294 (2019).

[53]H. Cho, H. Y. Kim, J. Y. Kang, and T. S. Kim, J. Colloid Interface Sci. **306**, 379–385 (2007).

[54]M. Zimmermann, P. Hunziker, and E. Delamarche, Microfluid. Nanofluid. **5**, 395–402 (2008).

[55]J. L. Moore, A. McCuiston, I. Mittendorf, R. Ottway, and R. D. Johnson, Microfluid. Nanofluid. **10**, 877–888 (2011).

[56]T. S. Leu and P. Y. Chang, Sens. Actuators A **115**, 508–515 (2004).

[57]L. Zhang, B. Jones, B. Majeed, Y. Nishiyama, Y. Okumura, and T. Stakenborg, J. Micromech. Microeng. **28**, 065005 (2018).

[58]S. X. Wang, X. F. Zhang, C. Ma, S. Yan, D. Inglis, and S. L. Feng, Biosensors **11**, 405 (2021).

[59]V. A. Papadimitriou, L. I. Segerink, A. van den Berg, and J. C. T. Eijkel, Anal. Chim. Acta **1000**, 232–238 (2018).

[60]A. Cazale, W. Sant, F. Ginot, J. C. Launay, G. Savourey, F. Revol-Cavalier, J. M. Lagarde, D. Heinry, J. Launay, and P. Temple-Boyer, Sens. Actuators B **225**, 1–9 (2016).

[61]M. Parrilla and K. De Wael, Adv. Funct. Mater. **31**, 2107042 (2021).

[62]M. Parrilla, M. Cuartero, and G. A. Crespo, TrAC **110**, 303–320 (2019).

[63]M. Bauer, L. Wunderlich, F. Weinzierl, Y. J. Lei, A. Duerkop, H. N. Alshareef, and A. J. Baeumner, Anal. Bioanal. Chem. **413**, 763–777 (2021).

[64]F. Poletti, B. Zanfrognini, L. Favaretto, V. Quintano, J. H. Sun, E. Treossi, M. Melucci, V. Palermo, and C. Zanardi, Sens. Actuators B **344**, 130253 (2021).

[65]M. Parrilla, I. Ortiz-Gómez, R. Cánovas, A. Salinas-Castillo, M. Cuartero, and G. A. Crespo, Anal. Chem. **91**, 8644–8651 (2019).

[66]J. Cirello-Egamino and I. D. Brindle, Analyst **120**, 183–186 (1995).

[67]A. Wiorek, M. Parrilla, M. Cuartero, and G. A. Crespo, Anal. Chem. **92**, 10153–10161 (2020).

[68]R. M. Torrente-Rodriguez, J. B. Tu, Y. R. Yang, J. H. Min, M. Q. Wang, Y. Song, Y. Yu, C. H. Xu, C. Ye, W. W. IsHak, and W. Gao, Matter **2**, 921–937 (2020).

[69]K. Kwon, J. U. Kim, Y. J. Deng, S. R. Krishnan, J. Choi, H. Jang, K. H. Lee, C. J. Su, I. Yoo, Y. X. Wu, L. Lipschultz, J. H. Kim, T. S. Chung, D. R. Wu, Y. Park, T. I. Kim, R. Ghaffari, S. Lee, Y. G. Huang, and J. A. Rogers, Nature Electronics **4**, 302–312 (2021).

[70]Z. Yang and S. Xia, J. Coast. Res. **104**, 504–507 (2020).
[71]D. M. Dipasquale, F. W. Kolkhorst, J. F. Nichols, and M. J. Buono, High Alt. Med. Biol. **3**, 289–292 (2002).
[72]F. J. V. F. F. White, Adv. Fluid Mech. **39**, 104–217 (1991).